*Final Draft*
**of the original manuscript:**

Cornec, A.; Schoenfeld, W.; Schwalbe, K.-H.; Scheider, I.:
**Application of the cohesive model for predicting the residual strength of a large scale fuselage structure with a two-bay crack**
In: Engineering Failure Analysis (2008) Elsevier

DOI: 10.1016/j.engfailanal.2008.10.014

Elsevier Editorial System(tm) for Engineering Failure Analysis
Manuscript Draft

Manuscript Number:

Title: Application of the Cohesive Model for Predicting the Residual Strength of a Large Scale Fuselage Structure with a Two-Bay Crack.

Article Type: Original Research Paper

Section/Category:

Keywords: Residual strength, riveted fuselage panel, ductile crack extension, finite element analysis, cohesive model

Corresponding Author: Dr. Alfred Cornec,

Corresponding Author's Institution: GKSS Research Centre

First Author: Alfred Cornec

Order of Authors: Alfred Cornec; Karl-Heinz Schwalbe, Prof.; Ingo Scheider; Wernfried Schönfeld

Manuscript Region of Origin:

# Application of the Cohesive Model for Predicting the Residual Strength of a Large Scale Fuselage Structure with a Two-Bay Crack

A. Cornec*, K.-H. Schwalbe, I. Scheider, W. Schönfeld

Institute of Materials Research,
GKSS Research Centre – Member of the Helmholtz Association,
Max-Planck-Strasse 1, D-21502 Geesthacht, Germany

---

## Abstract

The residual strength of a curved and stiffened panel containing a two-bay crack was assessed using the cohesive model. This panel represents a section of a wide-body aeroplane fuselage. The tests were conducted at IMA GmbH Dresden in cooperation with Airbus Industries Germany. The structural panel was modelled using 3D finite elements and a layer of cohesive elements ahead of each crack tip allowing for 70 mm crack extension. Identification of the cohesive parameters was done on small laboratory test pieces. Special effort was made for the transfer of these parameters to the structure. Reasonably conservative predictions of the residual strength of the panel were achieved. The boundary conditions of the loading devices of the test rig are shown to have substantial influence on the predictions.

*Key words:* Residual strength, riveted fuselage panel, ductile crack extension, finite element analysis, cohesive model

---

* Corresponding author. Tel.: +49-4152-87-2535; Fax: +49-4152-87-2534, E-mail address: cornec@gkss.de (A. Cornec).

**Nomenclature**

*Variables*

| | |
|---|---|
| $a_i$ | half crack length |
| $a_0$ | initial half crack length |
| $p_i$ | internal pressure |
| $w_0$ | initial width of flat bar specimen |
| $w_{\text{nec}}$ | necking width of flat bar specimen during tension loading |
| $t$ | thickness of the skin |
| $t_0$ | initial thickness of flat bar specimen |
| $t_{\text{nec}}$ | necking tickness of flat bar specimen during tension loading |
| | |
| CMOD | crack mouth opening displacement |
| CTOD | crack tip opening displacement |
| $F$ | force |
| $J_{\text{i}}$ | fracture toughness for crack initiation in terms of the *J*-integral |
| $R_{\text{p0.2}}$ | yield strength at 0.2% plastic strain |
| $R_0$ | outer radius of the fuselage |
| SZW | stretch zone width |
| $T(\delta)$ | traction-separation law (TSL) |
| $T_{0\text{N}}$ | cohesive strength for normal fracture |
| $T_{0\text{S}}$ | maximum cohesive traction for slant fracture |
| | |
| $\delta$ | separation |
| $\delta_0$ | critical cohesive separation |
| $\delta_1$, $\delta_2$ | shape parameters of TSL |
| $\delta_5$ | crack tip opening displacement across initial crack tip with 5 mm gauge length |
| | |
| $\Delta a$ | crack extension |
| $\Gamma_{0\text{N}}$ | cohesive energy for normal fracture |
| $\Gamma_{0\text{S}}$ | cohesive energy for slant fracture |

*Acronyms*

| | |
|---|---|
| C(T) | compact tension specimen |
| M(T) | middle cracked tensile panel |
| TSL | traction-separation law |

## 1. Introduction

The requirements for high loading capacity, weight reduction and low production cost of engineering structures, combined with high structural safety, particularly in transportation industry, have to be met by new design concepts, materials, production technologies, and assessment methods. When safety of a new airplane has to be demonstrated during the development stage, extremely expensive test programs are required. The residual strength of the fuselage, for instance, has to satisfy aerospace certification requirements. A longitudinal crack of twice the distance between two stiffeners is inserted into a full-scale barrel section representing the fuselage design which is then subjected to internal pressure [1]. The required residual strength of that cracked structure has to be at least 1.15 times the internal cabin pressure.

In order to reduce testing costs, Airbus in Germany in cooperation with IMA[1] have developed a new, cost-saving, test procedure for fuselages. Instead of a complete barrel, only a section of it is loaded by internal pressure and biaxial tension. The inner side of the IMA panel is sealed against a chamber so that internal pressure can be built up. Tests can be done under monotonically increasing and cyclic loads [2]. Although this test rig is quite complex, it allows testing a range of design solutions with much less efforts than the classical barrel test. Furthermore, simulations applying advanced models of fracture and damage mechanics would reduce test efforts even more, since as soon as the finite element model of a panel has been made up parameter variations with respect to geometrical parameters, boundary conditions and material properties can be effectively studied.

Thin-walled light-weight structures such as the fuselage of an aeroplane may exhibit a large amount of crack extension before final failure ensues. The ability of treating large amounts of ductile crack extension can in general be met by a number of assessment procedures and numerical models. It is common practice to treat ductile crack extension in the form of a crack extension resistance curve ($R$-curve), with crack extension expressed as a function of either of crack tip parameters like the stress intensity factor, $K$, the $J$ integral, or crack tip opening displacement (CTOD) [3]. Among CTOD the $\delta_5$ crack tip opening displacement method with a fixed gauge length at the crack tip is extensively validated for dealing with large amounts of crack extensions [4-8] and is now standardised by ASTM [9] and ISO [10].

[1] IMA GmbH Dresden in Germany (Materialforschung und Anwendungstechnik GmbH).

Besides these classical fracture mechanics methods, numerical damage mechanics models are being increasingly used. Their advantage over the classical fracture mechanics methods is that they avoid an intrinsic problem of the latter: The essential transferability problem inherent in fracture mechanics can be better handled by damage mechanics models.

Numerical damage models such as the cohesive model, see e.g. general overviews in [11-14] and its application to thin-walled structures in [15-20] or porous plasticity models, e.g. [21-24], have already been extensively validated by means of numerous tests on laboratory test pieces, e.g. [15-17, 25-27]. However, only few investigations can be found on the application to complex large scale structural components. e.g. [28]. Earlier investigations carried out on a realistic fuselage component are based on the crack tip opening angle (CTOA) [29].

In the work described in the present paper, the cohesive model was chosen for simulating the residual strength of a cracked large scale and stiffend structural component. This choice was motivated by the suitability of this model for analysing large amounts of crack extension, the cuurent lack of structural applications, and by the experience of our group with this model. In order to test the versatility of the cohesive model for structural behaviour, the results of a panel test performed by IMA were made available to the authors. This panel is shown in Fig. 1 and will henceforth be called “IMA panel”.

The paper starts with a description of the IMA panel test, as the details of the test setup are needed for the boundary conditions of the numerical model. Then the cohesive model applied in this paper is introduced in detail. A description of the determination of the various material parameters follows. The following section deals with the finite element model of the panel and the results of its deformation behaviour. The paper concludes with the lessons learned during this exercise. The following step-by-step procedure was set up:

(i) The tensile properties of all materials of the panel were experimentally determined.

(ii) Fracture mechanics tests were performed on modified Kahn specimens made of the skin material taken from the tested IMA panel. The test results – together with the tensile properties – served for determining the cohesive parameters.

(iii) With the thus generated cohesive parameters the load carrying behaviour of the IMA panel was analysed.

## 2. IMA panel test setup

### 2.1 Panel design

The IMA panel is part of a wide-body fuselage with an outer diameter of 5640 mm, Fig. 2a. Geometry and dimensions of the panel are shown in Fig. 2b. The 1.8 mm thick skin is stiffened by 7 frames (C1-C7) and 8 stringers (P1-P8). The details of the riveted design near the crack tip in frame C3 are displayed in Fig. 3. The frame assembly consisted of several components. The stringers are adhesively bonded to the skin, representing a specific feature of this fuselage design. The other parts are connected by rivets.

The boundary conditions in the panel test approximate the behaviour of a closed fuselage. The fuselage panel was bi-axially loaded, i.e. in circumferential and longitudinal directions, each with special load transfer by hydraulic actuators at the panel edges, which will be displayed later together with the FE model.

A two-bay crack in the skin was made by fatigue loading with a high maximum load representing the cabin pressure. Frame C4 was manually cut prior to fatiguing the defect. At the end of fatigue crack propagation, the crack tips were located in the rivet axis of C3 and C5. Due to the stiffness of the bay between stringer and frame the fatigue crack path was slightly curved.

### 2.2 Loading of the panel

*Internal pressure*

The internal pressure, $p_i$, was realised by a pressure chamber mounted underneath the inner side of the panel, whose outer edges are indicated in Fig. 2b. The crack was sealed using a poly-urethane foam.

*Longitudinal loading*[2]

The panel (Fig. 2b) was mounted vertically in the IMA panel test rig. At the bottom edge of the skin a centred single force was introduced by a rigid crosshead. A number of straps were attached to the circumference of the skin, which were connected to each crosshead by freely rotating bolts. One edge of the IMA panel was attached to a fixed crosshead, the opposite edge to the crosshead mounted on a hydraulic actuator (see Fig. 11, which will be discussed in more detail below). The stringers are smoothly tapered towards the

[2] The terms “longitudinal” and “circumferential” refer to the direction related to the fuselage.

skin edge. The longitudinal force in the panel test is the equilibrium force analytically determined for an internally pressurized closed cylinder.

*Circumferential loading*

The load transfer to the skin and frames in circumferential direction of the IMA fuselage panel was performed by flexible straps at the skin edge and a pin-joint at the end of the frames, each attached to freely rotating bolts mounted on hydraulic actuators as shown in Fig. 11. At the skin edge the hydraulic actuators were fixed during the panel test to generate reaction forces. All other forces applied in circumferential as well as longitudinal directions applied by hydraulic actuators increase proportionally with the internal pressure. The forces were calculated from the tangential stresses in a closed un-cracked vessel with frames under internal pressure. This means, that all frames (C1-C7) were loaded with equal forces.

## 3. Stress-strain data

The fuselage panel consisted of components made of five materials as specified in Fig. 4. The stress-strain curves were determined on the small flat tensile specimens, depicted in Fig. 4. Elongation was measured with a clip of 7.0 mm initial gauge length. The tensile specimens were taken from all components of the IMA panel.

Three of the stress-strain curves belong to one group, whose individual curves are similar, namely skin, clip and lower frame. The stringer and the upper frame profiles have significantly higher strengths. For all materials the elastic modulus was taken as $E$ = 68000 MPa and the Poisson' ratio, $\nu$, was 0.3. The yield strengths are listed in Tab.1.

| Part | Material | Thickness mm | Yield stress $R_{p0.2}$ MPa |
|---|---|---|---|
| Skin | 2524-T351 | 1.8 | 276.0 |
| Stringer | 7149-T76511 | 1.6 | 540.6 |
| Clip | 7475-T762 | 1.8 | 287.0 |
| Upper frame | 7075-T79511 | 2.5 | 475.0 |
| Lower frame | 7475-T762 | 2.0 | 296.2 |

Table 1. Parameters of the components of the panel.

For the skin material the true stress-strain curve was determined even beyond ultimate strength until unstable failure. This was done using optical instrumentation acquiring

digital images focused the necking region. For the determination of the displacement in that region the tensile specimen was coated by a titanium oxide spray in order to obtain a surface with distinctive points. The local strain, $\varepsilon_{\mathrm{loc}}$, in loading direction was determined from the displacements of two points with an initial base length, $L_{0,\mathrm{loc}} = 0.25$ mm. In addition, the area of the specimen in the necking region, $A_{\mathrm{nec}}$, was calculated based on the width reduction, $w_{\mathrm{nec}}$, determined from the images and the observation of almost equal necking ratios for width and thickness reduction: $w_{\mathrm{nec}}/w_0 = t_{\mathrm{nec}}/t_0$. This is valid for the used nearly square tensile bar section. For the tensile test used, the initial width was $w_0 = 2.02$ mm and the thickness was $t_0 = 1.78$ mm. From this test data, the true stress and strain was calculated by:

$$
\begin{aligned}
t_{\mathrm{nec}} &= \frac{w_{nec}}{w_0} t_0 \\
A_{\mathrm{nec}} &= w_{nec} t_{nec} \\
\varepsilon_{loc} &= \frac{\Delta L_{\mathrm{loc}}}{L_{0,\mathrm{loc}}} \\
\varepsilon_{\mathrm{true}} &= \ln\left(1 + \varepsilon_{\mathrm{loc}}\right) \\
\sigma_{\mathrm{true}} &= F \,/\, A_{\mathrm{nec}}
\end{aligned}
\tag{1}
$$

## 4. Cohesive Parameters

### 4.1 Traction-separation law

Cohesive models describe various kinds of decohesion processes by its constitutive behaviour, which is a relation between surface tractions, generally having one normal and two tangential components, and the corresponding material separations. In an FE model, the cohesive surface is introduced by interface elements at the boundaries of solid elements along a pre-defined crack path. Cohesive elements are surface elements in 3D structures and line elements in 2D structures. They do not have an initial thickness but nevertheless an upper and a lower surface with duplicated nodes, which can separate during loading.

Fig. 5a shows schematically the mode I fracture process in a ductile material and its idealisation by a cohesive model. It is assumed that all micro-structural mechanisms of the fracture process can be captured by two cohesive parameters, the maximum traction or cohesive strength, $T_0$, and a critical separation, $\delta_0$, beyond which the respective cohesive element has lost its stress carrying capacity, and the crack extends by one element length. Alternatively to $\delta_0$, the separation energy, $\Gamma_0$, being the integral under the

T($\delta$) curve, see Fig 5b, can be used as a cohesive parameter, as was done in the present study.

Various functions for the traction-separation law (TSL) have been proposed in the literature. Though the cohesive model is phenomenological, the TSL has to represent the micromechanical mechanisms of material separation. In the present analysis, a function as proposed in [30] is applied:

$$T = T_0 \cdot \begin{cases} 2\left(\frac{\delta_1}{\delta_0}\right) - \left(\frac{\delta_1}{\delta_0}\right)^2 & \text{for } \delta < \delta_1 \\ 1 & \text{for } \delta_1 < \delta < \delta_2 \\ 2\left(\frac{\delta - \delta_2}{\delta_0 - \delta_2}\right)^3 - 3\left(\frac{\delta - \delta_2}{\delta_0 - \delta_2}\right)^2 + 1 & \text{for } \delta_2 < \delta < \delta_0 \end{cases} \tag{2}$$

Besides the cohesive parameters $T_0$ and $\delta_0$, this TSL contains two additional shape parameters, $\delta_1$ and $\delta_2$, allowing for varying the shape of the curve. With this function, the cohesive energy, $\Gamma_0$, is related to $T_0$ and $\delta_0$ by

$$\Gamma_0 = \int_0^{\delta_0} T(\delta)\mathrm{d}\delta = \frac{1}{2} T_0 \delta_0 \left(1 - \frac{2}{3}\frac{\delta_1}{\delta_0} + \frac{\delta_2}{\delta_0}\right) \tag{3}$$

Fig. 5b shows the TSL for $\delta_1 = 0.01\delta_0$ and $\delta_1 = 0.5\delta_0$, which has proven to provide reasonable results for ductile crack extension [14,18,20].

### 4.2 Determination of the cohesive parameters

As already mentioned at the end of the introduction, some mechanical fracture mechanics tests are needed for determining the cohesive parameters. However, for the skin material no flat sheet of the same charge as that of the fuselage was available for this purpose. Therefore, two modified and fatigue pre-cracked Kahn specimens [31] as shown in Fig. **6** were fabricated from the skin material. Since the geometrical offset in this specimen is around 50 µm, It is believed that the curvature of the fuselage skin ($R_0$ = 2820 mm) can be tolerated in this case. During the test, the applied force, F, and the crack mouth opening displacement (CMOD), were measured**.**

In thin-walled structures, a crack usually starts its extension in a flat fracture mode, followed by slant fracture mode where the crack is inclined at 45° to the surface of the component, see Fig. 7d. Since the initial flat mode is very short compared to the amount

of crack extension achieved prior to instability of the component, it can be ignored in a structural analysis. Crack initiation will then occur slightly earlier. Thus, consideration of this initial flat portion for the determination of homogeneous cohesive parameters might not be necessary. Therefore, this is the usual way of performing cohesive model simulations in thin-walled structures, where slant fracture occurs [16,17,19].

However, it turned out that in the Kahn specimen the transition from flat to slant fracture was fully developed past maximum force. Thus, the extraction of the cohesive parameters from the Kahn specimen required also consideration of the initial flat mode to fit the load level due to the flat fracture part. Hence, four cohesive parameters had to be identified: $T_{0N}$, $\Gamma_{0N}$, $T_{0S}$, $\Gamma_{0S}$, with N for normal (mode I) and S for slant fracture (mixed mode I and III).

*Mode I fracture*

For mode I fracture, a procedure for the determination of the cohesive parameters has been proposed and validated in [14] which was also used in the present study. The cohesive strength for normal fracture, $T_{0N}$, can be identified as the maximum stress at failure of a deeply notched flat bar under tension (Fig. 6), which is determined from an elastic-plastic FE analysis, Fig. 7a, yielding $T_{0N}$ = 700 MPa at failure load. It has to be noted that the notched tensile specimen did not fail in a pure mode I fashion; a shear mode contribution was also present. Therefore, fine tuning of $T_{0N}$ was carried out as described below in the section on slant fracture.

In [14] it is also stated that the cohesive energy for normal fracture, $\Gamma_{0N}$, is equal to the $J$-integral at physical crack initiation in mode I, $J_i$, which is usually identified from a $J_R$-curve as the intersection point between the critical stretch zone width, $SZW_c$, determined from the fracture surface and the $J_R$-curve. As in this project no $J_R$-curve was available, an alternative procedure was applied: $J_i$ was taken from the intersection of the critical stretch zone, $SZW_c$, with the blunting line, which according to [9, 32] is given by a validated analytical solution. The principle is shown in Fig. 7b and yielded $\Gamma_{0N}$ = 40 N/mm for an average value of $SZW_c$ = 25 µm. This $SZW_c$ was determined from scanning electron microscope images of the initial fracture surface of the tested Kahn specimen.

*Slant fracture*

In the present study, slant fracture is treated like a mode-I fracture (normal separation) with the fracture plane normal to the applied load and appropriate "effective" cohesive parameters. The cohesive traction for slant fracture, $T_{0S}$, was determined experimentally from the flat, smooth, tensile bar shown in Fig. 6. At the end of the test sudden failure

occurred as slant fracture across the thickness. The true stress at failure as calculated by the force at failure divided by the actual cross section of the specimen was then set equal to the cohesive traction, resulting in $T_{0S}$ = 610 MPa.

In contrast to normal fracture, no independent method for determining the cohesive energy for slant fracture is available. Therefore, the cohesive energy, $\Gamma_{0S}$, was determined by a finite element crack extension analysis of the two Kahn specimens tested, based on the cohesive model using the three previously determined parameters $T_{0N}$ , $\Gamma_{0N}$ and $T_{0S}$. The 3D FE mesh consisted of linear hexahedral elements. The cohesive elements along the ligament had a width of 0.125 mm and a thickness of 0.3 mm, thus the element size was in the order of the maximum separation $\delta_0$. The region, where the parameters for mode I fracture were applied, is shown in the small sketch inserted in Fig. 8, in which this simulation is denoted as “normal+slant”. Comparing the thus simulated force-crack mouth opening displacement (*F*-CMOD) curve with the experimental ones yielded $\Gamma_{0S}$ = 25 N/mm, see Fig. 8.

The test served also for fine tuning the cohesive strength for normal fracture, resulting in a final value of $T_{0N}$ = 660 MPa which is quite close to the original approximated value of 700 MPa anticipated by the notched tensile bar.

*Justification of the transition region for the parameter identification*

In Fig. 8 a further analysis is depicted: Since – as mentioned above – in a large structure the normal fracture mode plays only a marginal role and is usually neglected, the behaviour of the Kahn specimens was also homogeneously simulated using only the parameters for slant fracture determined above ($T_{0S}$ = 610 MPa and $\Gamma_{0S}$ = 25 kJ/m²). It is seen that this simulation, in Fig. 8 called “slant 1”, provides a curve substantially below the first one obove.

In addition, a second run for identifying homogeneouse cohesive parameters ignoring mode I fractute was performed: The complete experimental *F*-CMOD curve was fitted and yielded $T_0$ = 518 MPa and $\Gamma_0$ = 55 kJ/m². This simulation shown in Fig. 8 is labelled “slant 2” and is very close to the experimental curves as well as the first one ("normal+slant"). Table 2 summarizes all cohesive parameters for the three simulatons.

| Simulation | Normal fracture | | Slant fracture | |
|---|---|---|---|---|
| | $T_{0N}$ MPa | $\Gamma_{0N}$ kJ/m² | $T_{0S}$ MPa | $\Gamma_{0S}$ kJ/m² |
| Normal + Slant | 660 | 40 | 610 | 25 |
| Slant 1 | - | - | 610 | 25 |
| Slant 2 | - | - | 518 | 55 |

Table 2: Cohesive model parameters identified for the skin material.

Furthermore, in a pure numerical study, the transferability problem from a small specimen to a large structure is illustrated by an additional 3D FE exercise on a large fracture specimen, namely a C(T) specimen of 1000 mm width and 1.8 mm skin thickness. Of course, it can be assumed that the region a few millimetres ahead of the initial crack tip, i.e. the mode I fracture part, has a negligible influence on the global response, here expressed by F-CMOD curves.

A comparison between a simulation with the original heterogeneous parameters $T_{0N}$, $\Gamma_{0N}$, $T_{0S}$, $\Gamma_{0S}$ ("normal+slant") and homogeneous "slant 1" parameters yields negligible difference, see the *F*-CMOD curve in Fig. 9. However, if the optimized homogeneous parameters for "slant 2" are used, which yielded equal *F*-CMOD response compared to the heterogeneous simulation "normal+slant" in case of the Kahn specimen (Fig. 8), but one can see now, that the *F*-CMOD curve for "slant 2" is far away from the other simulations. Thus, homogeneous cohesive parameters determined on small specimens are not applicable for larger structures.

## 5. Finite element model of the IMA panel

### 5.1 FE mesh

A 3D CAD was generated and meshed using the programme IDEAS[3]. All construction profiles are connected by rivet blocks, see Fig. 10a. The two-bay crack was manually inserted. The FE model consisted of 77208 solid elements with 551086 nodes. The elements had 20 nodes and 8 integration points (ABAQUS type C3D20R). A refined crack tip mesh block was placed at each of the two crack tips.

Cohesive elements were inserted ahead of both crack tips, in axial direction with an element width of 0.2 mm and a length equal to the skin thickness, see Fig. 10b. An element set for normal fracture is considered at the crack front similar as done for the

[3] Product of Unigraphics Solutions

Kahn specimen as shown in Fig. 8. Each crack tip region contained 702 quadratic cohesive elements with 16 nodes over a distance of about 70 mm ahead of the crack tips.

The finite element analyses were run on a HP workstation X4000. The runs for the panel model took up to four weeks.

### 5.2 Loading and boundary conditions

Loading of the panel was performed numerically as follows:

(i) The internal pressure, $p_i$, was equally distributed over the skin surface and normal to the surface, Fig. 11a. The pressurized area is indicated in Fig. 2. The pressure was applied linearly increasing over time until the simulation failed to converge numerically. Such instability occurs in all load driven tests, whereas stability is easier to achieve in a displacement controlled test. A method to circumvent this problem is the modified RIKS algorithm implemented in the finite element system ABAQUS/Standard®, in which the applied stress and the corresponding displacement at the boundary are solved simultaneously by an arc length method. However, this algorithm is not applicable to such complex structures for numerical reasons and thus the maximum pressure can only be determined indirectly by loss of convergence.

(ii) The equilibrium force of the closed, un-cracked, fuselage was applied as a concentrated force at the left edge of the panel, with an additional constraint condition such that constant displacement along the edge was achieved, see Fig. 11a. This point force was proportional to the internal pressure. The right edge of the panel was kept fixed in longitudinal direction, however, free to move in radial and circumferential directions. For kinematic reasons the central node was fixed in circumferential direction.

(iii) Further boundary conditions at the skin and at the frame edges were applied in circumferential direction. At the skin edge a 380 mm long rigid rod was attached to the upper nodes of the solid elements, which rotate around the fixed support. The boundary conditions induce reaction forces along the skin edge. For frame loading two limit cases, denoted case A and B, were considered.

Case A: The frame edge is loaded in the same way as the skin edge with a sliding support around the centre point of a 400 mm long rotating rigid rod, Fig. 11b. Reaction forces will occur at the frame edges.

Case B: Instead of applying boundary conditions at the frame, concentrated forces are applied to all frame edges, Fig. 11c. This case was realised in the test. The force increases with the internal pressure and results from the equilibrium force of the closed un-cracked fuselage. However, it should be recognized that the forces in the frames of the cracked fuselage will be different and particularly vary at different positions in longitudinal direction.

### 5.3 Material properties in the FE model

In the FE model, the stress-strain curve of the skin identified in Section 3 was used for the whole assembly. As the finite element analysis has demonstrated, this simplification does not affect the deformation behaviour of the fuselage panel because the equivalent stresses in the stringers and upper frame profiles adjacent to the crack tips do not significantly exceed the yield strength of the skin, see later in Fig. 13. The rivets were also assigned the properties of the skin material.

## 6. Results and Discussion

### 6.1 Deformation and plastic zone extension

First, the global deformation and the distribution of plastic zones are presented, as determined at the failure pressure of the test and for the initial crack length. The largest deformation appears along the free edges of the two-bay crack as depicted in Fig. 12a, with two maxima in the middle of the two bays. Most important for the understanding of the deformation behaviour and the evaluation of the boundary conditions is the radial deformation along frame C4, shown in Fig. 12b for case A and in Fig. 12c for case B. All deformations are magnified by a factor of 10.

In case A the radial deformation in the centre of the two-bay crack is significantly lower than in case B. Correspondingly, the reaction force at the end of frame C4 in case A is by a factor of 1.85 higher compared to case B with equally distributed forces at the edges of the frames according to an un-cracked fuselage. In case A only the forces at the frame edges at the end of the panel, C1 and C7, approach the values as actively applied to all frames in case B.

In contrast to case B, the radial deformation in case A approaches gradually that of a complete fuselage. Therefore, the deformation pattern in case A appears to be more representative of a closed (full circumference) cracked fuselage**.**

Nevertheless, the boundary conditions of case A do not perfectly represent the complete cracked fuselage, since no circumferential displacements are possible at the end of the frames. However, this constraint condition yields the highest forces in the frames (as well at the skin edges), which accounts for the lowest radial displacements (see Fig. 12b). Lower radial displacements are related also to lower crack opening displacements. Thus, case A approaches an upper residual strength level.

On the other hand, case B (also equivalent to the panel test arrangement) is expected to yield a result which is conservative with respect to a complete two-bay cracked fuselage, since the equal forces for all frames yield the largest radial displacements (see Fig. 12(c)) which are related to a lower residual strength level. Thus case A and B enclose in principle the margin of the residual strength.

From this study one can see that the way of conducting the panel test does not fully represent the conditions in the complete fuselage, since the length of the circumference is too short and the effect of the crack has not yet vanished in the 45° section (Fig. 2a), if one takes the analogy of an M(T) panel, where the length of the panel must be at least 1.5 times the width of the panel in order to obtain results independent of the specimen size.

The plastic zones at frame C3 between stringers P3 and P4 are presented in Fig. 13 as outside and inside views for the initial crack length and at the load level $p_i = p_{i,test,max.}$ The highest iso-line value shows the plastic zone extension, i.e. the equivalent stress for the yield strength, $R_{p0.2} = 276$ MPa. One can see that plasticity occurs mainly in the skin, but also in the stringer, the clip foot and the rivets that join the clip to the skin. However, it should be noted that all parts have been simulated with the stress-strain curve of the skin. While in the real panel the plastic properties of the clip are very similar to that of the skin (see Fig. 4), the yield strength of the stringer is much higher, and this part only would actually be elastic. As the region of the plastic zone in the stringer is so small, that any error due to this inaccuracy can be neglected.

Significant plastification occurs as well across the clip rivets, particularly pronounced at the rivet adjacent to the crack tips, close to stringer P4, Since the plastic properties of the rivets could not be tested and thus are not known, again the properties of the skin have been applied. It can be assumed, however, that the real strength of the rivets is higher than that of the skin, so that the crack shielding effect associated with the rivets is in principle underestimated.

### 6.2 Residual strength

The residual strength (here expressed by the maximum internal pressure) as predicted with the cohesive simulation for case A is shown in Fig. 14. Instead of providing only a residual strength value, the complete pressure versus crack extension curves ($p_i$-$\Delta a$) are presented for the crack tips in frame C3 and C5, repectively.

The two crack tips propagate slightly differently due to the unsymmetrical composition of the frames below the crack tips (Fig. 3). The final point of the curve in Fig. 14 is the state where no numerical convergence could be achieved anymore, even though the time increments are reduced significantly. This end point indicates unstable failure of the structure, i.e. sudden collapse of a significant portion of the structure. The numerical loss of convergence is mechanically interpreted as equivalent to the physical instability of the panel test. This was validated on small specimens at maximum load level under load controlled condition. Simular experience regarding simulation of unstable failure is also described in [33].

The pressure-crack extension ($p_i$-$\Delta a$) behaviour for case B, which is the relevant case for the panel test, is shown in Fig. 15. From this figure, one can see the distinct effect of the boundary conditions of case A and B. The maximum pressure prediction is lower than for case A (about 9%) and shows a difference of 21% to the panel test. Crack initiation occurs at an earlier stage as well. This residual strength reduction is as well consistent with the interpretation of the radial deformations (Fig. 12b,c) as described above.

The reason for the distinct difference to the panel test can be contributed by a number of parameters within meshing, boundary conditions, material properties, idealizaton of the cohesive model, preloading history, and failure type. Among these basic items, some contributions in the panel test may be particularly involved, which are not contained in the simulations:

1. The accuracy of the meshing could have an influence on the structural response. Even though the effect of the length of cohesive elements in crack extension direction has already been proven to be small if the elements are small enough to capture the stress gradients in that direction; however, one element in thickness direction seems relatively coarse to capture the stress state in the out-of-plane direction accurately. It can be shown that a refined modelling change the local stiffness of the structure, which may alter the crack growth rate slightly, as the cohesive strength follows the stress gradient more gradually and the cohesive elements fails differently, either slower or faster. On the other hand, the increase of the number of elements along both

ligaments would significantly increase the model size and thus computational run time, which could not be handled during this project.

2. Even though the boundary conditions have been modelled carefully, the connection of the actuators to the structure is almost perfectly represented: The flexible straps are not modelled and the skin edge is directly connected to rigid rotating rods. A possible minor influence of the additional compliance is not known.

3. The rivets have a significant shielding effect towards the crack opening profile. The use of the single stress-stress curve from the skin instead of an elastic or even rigid rivet behaviour provides obviously significant conservative predictions. From additional elastic-plastic FE calculations of the IMA panel (without stable crack extension) it was found that rigid rivets enhance the load capacity of about 10% compared to the skin-rivet behaviour, determined at the same CTOD values. Simular, for a stationary crack (at equal CTOD values) the load for case A is about 10% higher than for case B and the residual strength form the simulation with crack extension is as well of the same order higher (Fig. 15). Therefore it can be expected, that rigid rivet behaviour (in particular the rivets close to the crack tips) will significantly increase the residual strength of the panel of approximately 10%.

4. Cyclic preloading, prior to the residual strength test, have also an important effect on the evolution of the crack extension, which was not yet considered in the simulations above. As mentioned already, from a saw cut the crack was extended by cyclic loading between zero and cabin pressure. This preloading leads to plastic deformation ahead of the crack tips, and the crack closure effect after unloading is beneficial for the subsequent strength of the fuselage panel. This aspect has been investigated by an additional simulation with one preloading step (ramp loading up to cabin pressure and unloading to zero pressure) starting with a crack tip at about 8 mm before the rivet axes in C3 and C5, respectively. During the first loading up to cabin pressure the crack extends and reaches the rivet axes and after unloading the initial situation of the residual strength test is equivalently conducted in the simulation. The subsequent reloading runs till unstable failure. Fig. 16a shows the load sequence for the panel test together with the single preloading step in the simulation. The complete pressure-crack extension ($p_i$-$\Delta a$) curves with and without preloading is depicted in Fig. 16b. Even though the curve is shown for case A only, which is not the one with the boundary condition relevant for the panel test[4], one can see that preloading in

[4] The investigation has been performed before it was found out that case B reproduces the testing conditions better, but afterwards no more time for the long simulation was left.

principle increases the pressure at failure at leat by 6%. This is mainly due to the fact that crack extension starts at a much higher internal pressure compared to the simulation without preloading. One can also see that crack extension before unstable failure is much lower for the preloaded panel.

5. The idealization of the cohesive model does not consider the real slant fracture in a thin-wall structure (under 45° across the thickness). Crack extension is modelled in the projection plane equivalent to normal fracture but with cohesive parameters consistently determined as well in the projection plane. However, the real slant crack extension may be affected differently, particularly in combination with bulging of the crack flanks, compared to the projection plane of the cohesive model,.

## 7. Conclusions

A residual strength analysis of a curved fuselage panel with riveted-on frames containing a two-bay crack has been successfully conducted using a 3D FE analysis in combination with the cohesive model. The main conclusions from this study are as follows.

- A hybrid method combining experiments and simulations for determining the cohesive parameters of a thin-walled Aluminium sheet with combined normal and slant fracture modes is verified and sucessfully applied to the fuselage panel.
- It has been shown in a numerical study that for small specimens the first part, where the crack extends in pure mode I conditions before it turns into the slant fracture mode, cannot be neglected for small specimens, but does not significantly affect the response of the large structures. A homogenous fit to small specimen response (load-displacment) are not applicable cohesive parameters for large crack extension with slant fracture.
- The 3D crack extension simulation of a complex fuselage panel using the cohesive model is robust and able to predict crack extension of several centimetres (leading to more than 300 failed cohesive elements).
- The residual strength (pressure) was too conservative with respect to the panel test. Five effects are pointed out to understand the predicted conservatism.
- High preloading has a dominant effect on the structural response: Residual strength increases while crack extension at unstable failure decreases compared to non-preloading. For reasonable predictions this must be taken into account.

- The influence of the boundary conditions has been studied by two different loading types at the frames edges. It has been shown, that the IMA panel is not sufficiently extended in circumferential direction to achieve the realistic boundary conditions of a complete cracked fuselage barrel.
- The simulation with the cohesive model provides the onset of unstable failure by loss of convergence. This is an important aspect for large structures, which typically fail unstable. Failure of a rivet panel can also be activated by rivet failure (here in particular at the crack tips in the frame axes C3 and C5). With careful rivet meshing the presented cohesive model could also be applied.
- The simulation can be used to substitute the very expensive panel tests for design studies, or to improve the design of this kind of panel tests.

The main goal of the presentations should demonstrate the applicability of the cohesive model for predicting large and complex structural behaviour including unstable failure. The conservative assumptions made should provide the margin of under-estimation of residual strength prediction. Form the experience made above, it is expected that fine-tuning of the relevant parameters the simulations will realistically approach the fuselage behaviour.

## Acknowledgments

Authors gratefully acknowledge Dr. H.-J. Schmidt and Dr. Assler with Airbus Deutschland in Hamburg as well Dr. T. Fleischer and Dipl.-Ing. M. Semsch with IMA Materialforschungs- und –anwendungstechnik GmbH in Dresden for their kind cooperation and support of this study with valuable information on the fuselage test setup. Our colleague Dipl.-Ing. V. Heitmann is gratefully appreciated for supporting experiments on small specimens.

## References


[1] H.-J. Schmidt. Damage tolerance technology for current and future aircraft structure. Proceedings of the 23rd ICAF Symposium of the International Committee on Aeronautical Fatigue (Ed. Dalle-Donne), 8-10 June 2005, Hamburg Vol. I, p. 1-41.

[2] Fleischer T, Sachse M, Semsch M. Engineering approach and results of pressurized fuselage panel testing. Proceedings of the 23rd ICAF Symposium of the International Committee on Aeronautical Fatigue (Ed. Dalle-Donne), 8-10 June 2005, Hamburg Vol. I, p. 219-227.

[3] Zerst U, Heinimann M, Dalle-Donne C, Steglich D., Fracture and damage mechanics modelling of thin-walled structures – An overwiew. Eng Fract Mech 2007; doi:10.1016/j.engfracmech.2007.10.005.

[4] Schwalbe K-H, Zerbst U, Brocks W, Cornec A, Heerens J, Amstutz H. The ETM method for assessing the significance of crack-like defects in engineering structures. Fat Fract Engng Mat Struct 1998;21:1215-1231.

[5] Schödel M, Zerbst U. Application of the European flaw assessment procedure SINTAP to thin wall structures: analytical assessment levels. Eng Fract Mech 2004;71:1035-1058.

[6] Zerbst U, Schödel M, Webster S, Ainsworth R A. Fitness-for-service fracture assessment of structures containing cracks – A workbook based on the European SINTAP/FITNET Procedure. Elesevier, in press (to be appear in 2007).

[7] Schwalbe K-H. Heerens J, Zerbst U, Pisarski H, Koçak M. EFAM GTP 02 – the GKSS test procedure for determining the fracture behaviour of materials. GKSS Report 2002/24, GKSS Research Center Geesthacht, 2002.

[8] Zerbst U, Brocks W, Heerens J, Schödel M, Scheider I, Steglich D, Seib E, Cornec A, Schwalbe K-H. Failure assessment concepts for thin-walled structures. Proceedings of the 23rd ICAF Symposium of the International Committee on Aeronautical Fatigue, 2005, Hamburg, Ed. Dalle-Donne C, Vol. I, p. 161-175. 2005.

[9] ASTM E 2472-06, Test Method for Determination of Resistance to Stable Crack Extension under Low-Constraint Conditions, Annual Book of ASTM Standards, Vol. 03.01, ASTM International, West Conshohocken, Pa, USA, 2007.

[10] ISO 22889:2007, Metallic materials - Method of test for the determination of resistance to stable crack extension using specimens of low constraint, International Institute of Standardisation, Geneva, Switzerland, 2007.

[11] Borst R. Numerical aspects of cohesive-zone models. Eng Fract Mech 2003;70:1743-1757.

[12] Brocks W, Cornec A, Scheider I. Computational aspect of nonlinear fracture mechanics. In: Milne I, Ritchie RO, Karihaloo B, editors. Comprehensive structural integrity, vol 3. Amsterdam: Elesevier Science Publication; 2003. p. 127-209.

[13] Elices M, Guinea GV, Gòmez J, Planas J. The cohesive zone model: advantages, limitations and challenges. Eng Fract Mech 2002;69:137-163.

[14] Cornec A, Scheider I, Schwalbe K-H. On the practical application of the cohesive model. Eng Fract Mech 2003;70:1963-1987.

[15] Roy Y A, Dodds R H jr. Simulation of ductile crack growth in thin aluminum panels using 3-D surface cohesive elements. Int J Fract 2001;110:21-45.

[16] Li W, Siegmund T. An analysis of crack growth in thin-sheet metal via a cohesive zone model. Eng Fract Mech 2002;69:2073-2093.

[17] Chabanet O, Steglich D, Besson J, Heitmann V, Hellmann D, Brocks W. Predicting crack growth resistance of aluminium sheets. Comp Mat Sci 2003;26:1-12.

[18] Scheider I, Schödel M, Brocks W, Schönfeld W. Crack propagation analyses with CTOA and cohesive model: Comparison and experimental validation. Eng Fract Mech 2006;73:252-263.

[19] Scheider I, Brocks W. Cohesive elements for thin-walled structures. Comp Mat Sci 2006;37:101-109.

[20] Brocks W, Scheider I, Schödel M.Simulation of crack extension in shell structures and prediction of residual strength. Arch Appl Mech 2006;76:655-665.

[21] Tvergaard V, Needleman A., Analysis of the cup-cone fracture in around tensile bar. Acta Metall 1984;32:157-169.

[22] Rousselier, G., Ductile fracture models and their potential in local approach of fracture. Nucl Eng Des 1987;105:97-111.

[23] Gologanu M et al., Recent extensions of Gurson's model for porous ductile material, in Continuum Micromechanics. 1996, CISM, Udine.

[24] Reusch F, Svendsen B, and Klingbeil D, A non-local extension of Gurson-based ductile damage modeling. Comput Mater Sci 2003;26:219-229.

[25] Lin G, Cornec A, Schwalbe K-H. Three-dimensional finite element simulation of crack extension in aluminium alloy 2024-FC. Fat Fract Engng Mat Struct 1998;21:1159-1173.

[26] P. Nègre, D. Steglich, W. Brocks: Crack extension in aluminium welds: a numerical approach using the Gurson–Tvergaard–Needleman model, Eng. Fract. Mech. 71, 2004, 2365-2383.

[27] Jinkook Kim, Guihua Zhang, Xiaosheng Gao, Modeling of ductile fracture: Application of the mechanism-based concepts, Int. J. Solids Struct., 44, 2007, 1844-1862

[28] Scheider I. Residual stength prediction of a complex structure using crack extension analyses. Eng Frac Mech 2008;75:4001-4017.

[29] Chen C-S, Wawrzynek P A, Ingraffea A R. A methodology for fatigue crack growth and residual strength prediction with applications to aircraft fuselages. Comp Mech 1997; 19:527-532.

[30] Scheider I, Brocks W. Simulation of cup-cone fracture using the cohesive model. Eng Fract Mech 2003;70:1943-1961.

[31] Annual Book of ASTM Standards: ASTM B 871-96. Standard test method for tear testing of aluminum alloy products. The American Society for Tessting and Materials, West Conshohocken, USA, 1996.

[32] Schwalbe K-H, Hayes B, Baustian K, Cornec A, Gordon R, Homayun M, Voss B. Validation of the fracture mechanics tesst method EGF P1-87D (ESIS P1-90/ESIS P1-92). Fat Fract Engng Mat Struct 1993;16:1231-1284.

[33] Kabir R, Cornec A, Brocks W. Simulaton of quasi-brittle fracture of lamellar γTiAl using the cohesive model and a stochastic approach. Comp Mater Sci 2007;39:75-84.

**Figure captions**

Fig. 1. Inside view of the IMA fuselage panel after the test, last frame part C7 was detached after the test.

Fig. 2. IMA fuselage panel: (a) panel section as part of the wide-body complete fuselage; (b) fuselage panel dimension with frames, stringers, biaxial loading, pressure border, and two-bay crack.

Fig. 3. Detail of the riveted built-up parts from different aluminium alloys and the rivet arrangements. The numbers are the used notation for the different construction parts: 1 = skin, 2 = stringer, 3 = clip, 4 = upper frame, 5 = lower frame.

Fig. 4. Stress-strain relations of the different built-up parts from flat bar tensile tests; the true stress-strain curve of the skin is also determined locally until unstable failure.

Fig. 5. General aspects of the cohesive model: (a) real ductile fracture and idealization with the cohesive model; (b) deformation and fracture with solid and cohesive elements, respectively, and the specified traction-separation law used in this study.

Fig. 6. Specimen used for identification the cohesive parameters for normal and slant fracture.

Fig. 7. Determination of the cohesive parameter for the 1.8 mm thick skin material 2524-T351: (a) $T_{0N}$ from deeply notched flat bar tensile specimen; (b) $\Gamma_{0N}$ from a standardized procedure using analytical formulation and stretch zone width from fracture surface; (c) $T_{0S}$ experimentally determined value from smooth flat bar tensile specimen including necking effect; (d) $\Gamma_{0S}$ from cohesive simulation of a precracked Kahn specimen together with the otherwise determined parameters.

Fig. 8. Cohesive parameters optimized by accurate fitting the experimental load-displacement curve ($F$-CMOD) of the precracked Kahn specimen with large stable crack extension.

Fig. 9. Cohesive simulations providing $F$-CMOD curves on large C(T) specimen (W = 1000 mm, B = 1.8 mm, $a_0$ = W/2) for three different cohesive parameter sets.

Fig. 10. 3D solid mesh of the IMA fuselage panel; (a) frame mesh consisting of repeating units, all with inserted rivet blocks; (b) mesh detail at the crack-tips together with the cohesive elements ahead into the skin.

Fig. 11. Boundary conditions of the IMA fuselage panel: (a) pressure $p_i$ applied on the outside of the panel; (b) boundaries of case A with reaction forces on frame and skin edges; (c) mixed boundaries of case B with equal forces at all frame edges and reaction forces at the skin edge as used in the test.

Fig. 12. Deformation pattern of the IMA fuselage panel at the reference load $p_i/p_{i,max,test} = 1$ and for a stationary crack: (a) overview of the outside deformation of case A; (b) deformation of frame C4 for case A; (c) deformation of frame C4 for case B (all deformations are 10-fold enlarged).

Fig. 13. Equivalent stress distribution and the corresponding plastic zones at the reference load $p_i/p_{i,max,test} = 1$ at frame C3: (a) outside view; (b) inside view. Elastic-plastic FE results of a stationary crack (without cohesive elements).

Fig. 14. Cohesive simulation for case A: normalized pressure versus crack extension at frames C3 and C5.

Fig. 15. Cohesive simulation for case A and B: normalized pressure versus crack extension at frame C3.

Fig. 16. Effect of a preloading on residual strength; (a) test situation with fatigue preloading together with a single overload considered in the cohesive simulation starting at a crack-tip 8 mm before the frame axes C3 and C5, respectively; (b) comparison of cohesive simulations vor case A with and without preloading.

**Figures**

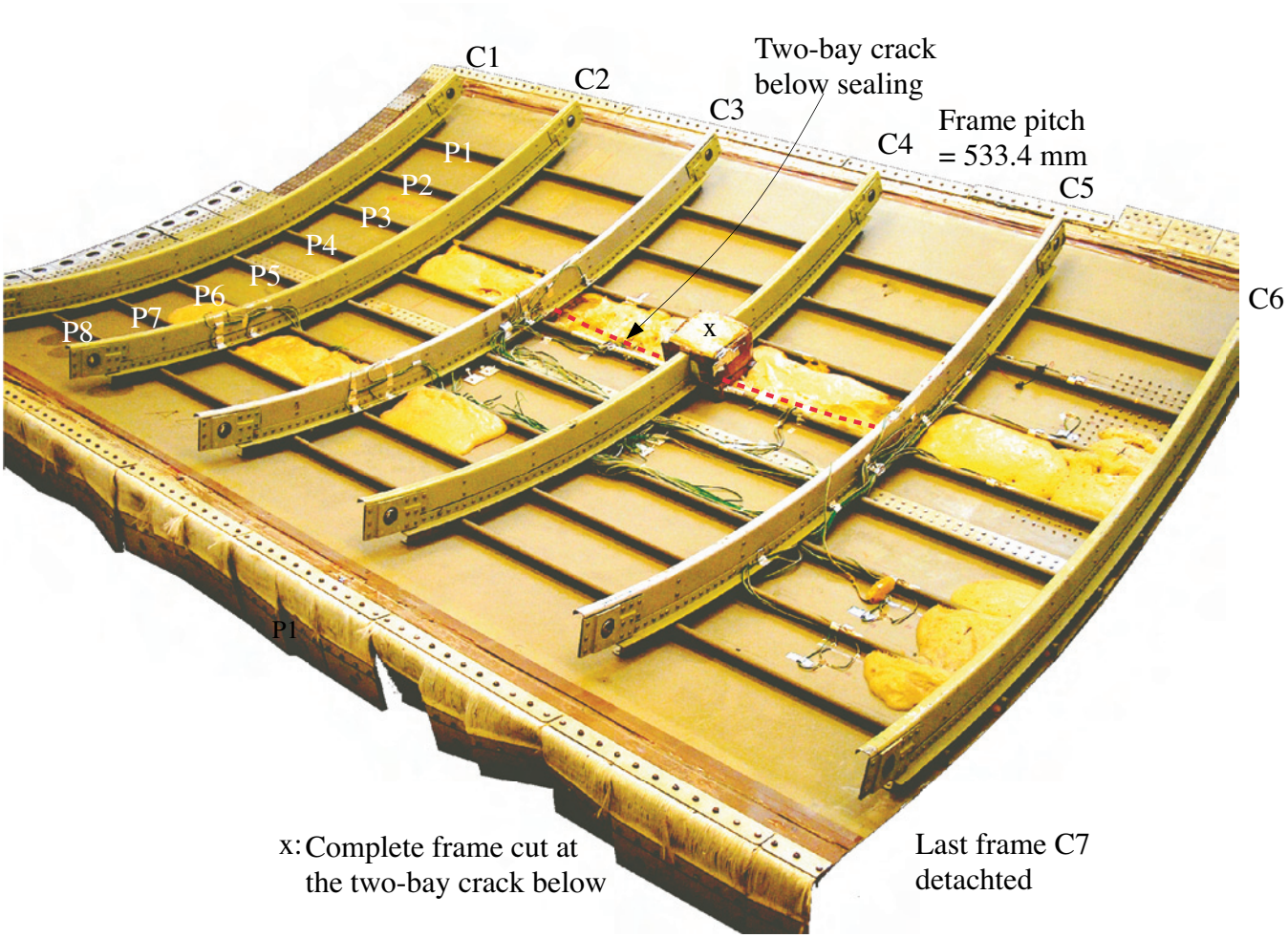


Fig. 1

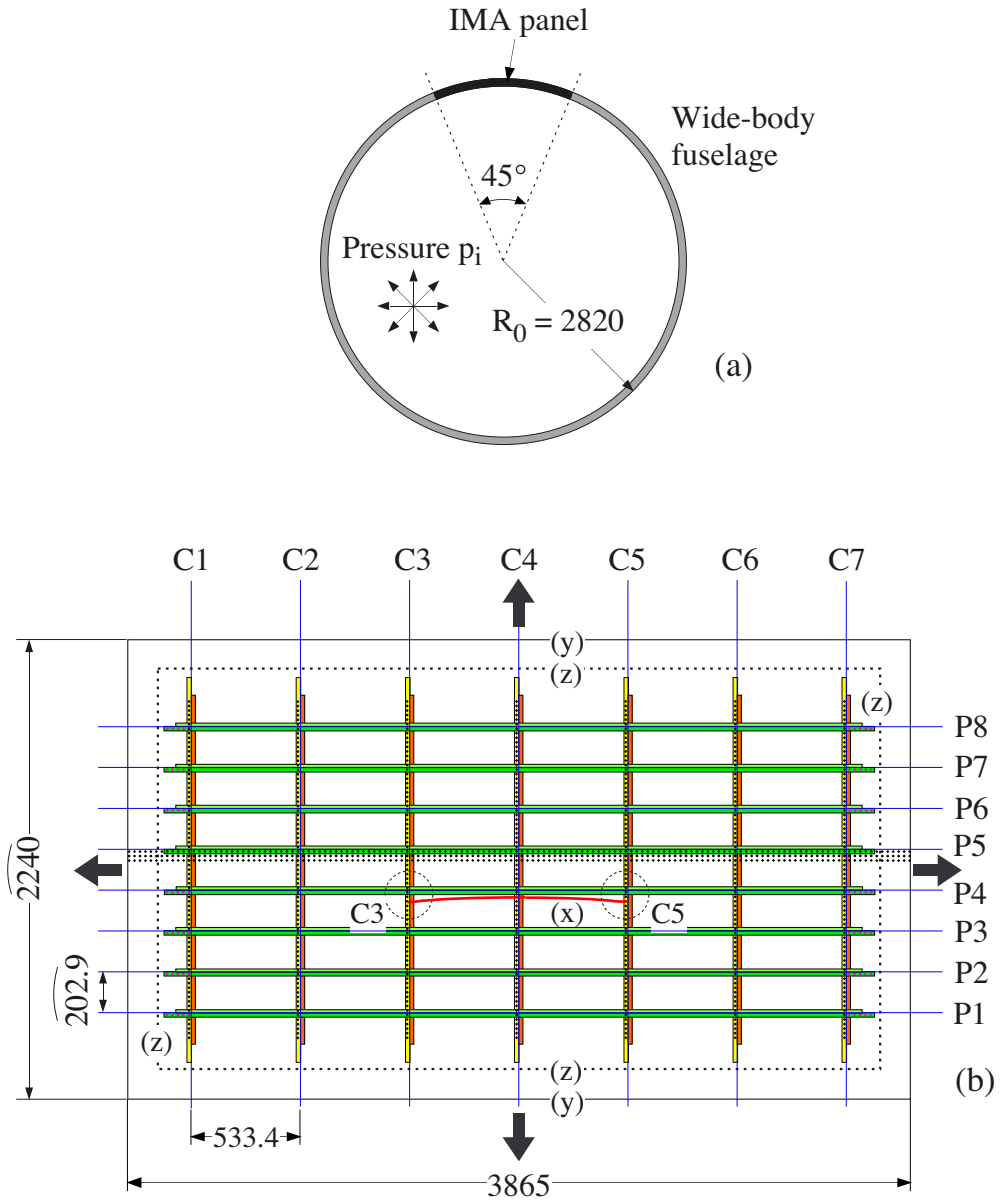


(x) Two-bay crack, (y) outer edges of the IMA panel,
(z) pressure area inside

Fig. 2

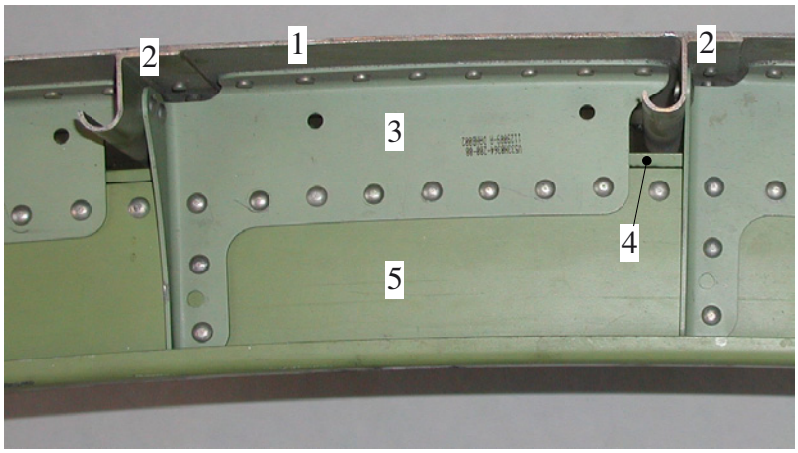


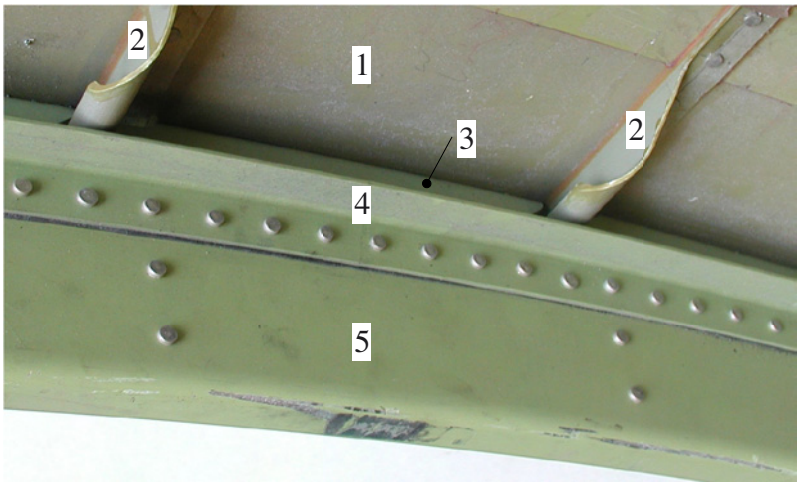


Fig. 3

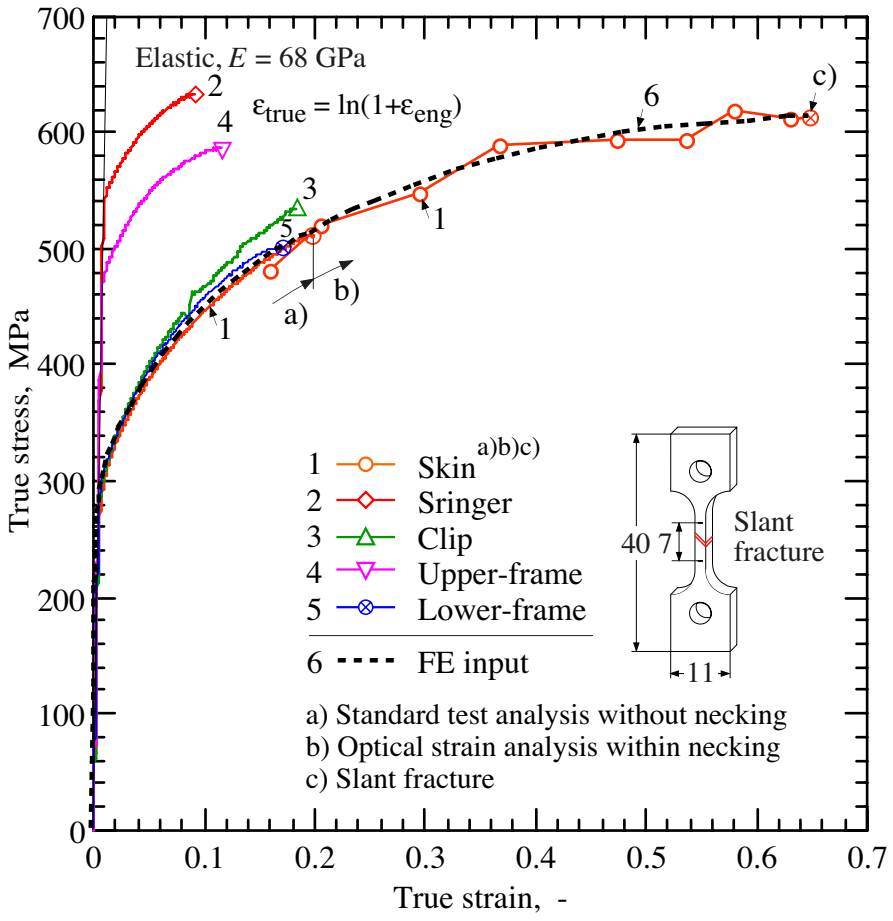
Elastic, E = 68 GPa
εtrue = ln(1+εeng)
True stress, MPa
True strain, -
1 Skin a)b)c)
2 Sringer
3 Clip
4 Upper-frame
5 Lower-frame
6 FE input
a) Standard test analysis without necking
b) Optical strain analysis within necking
c) Slant fracture
Slant fracture
40
7
11

Fig. 4

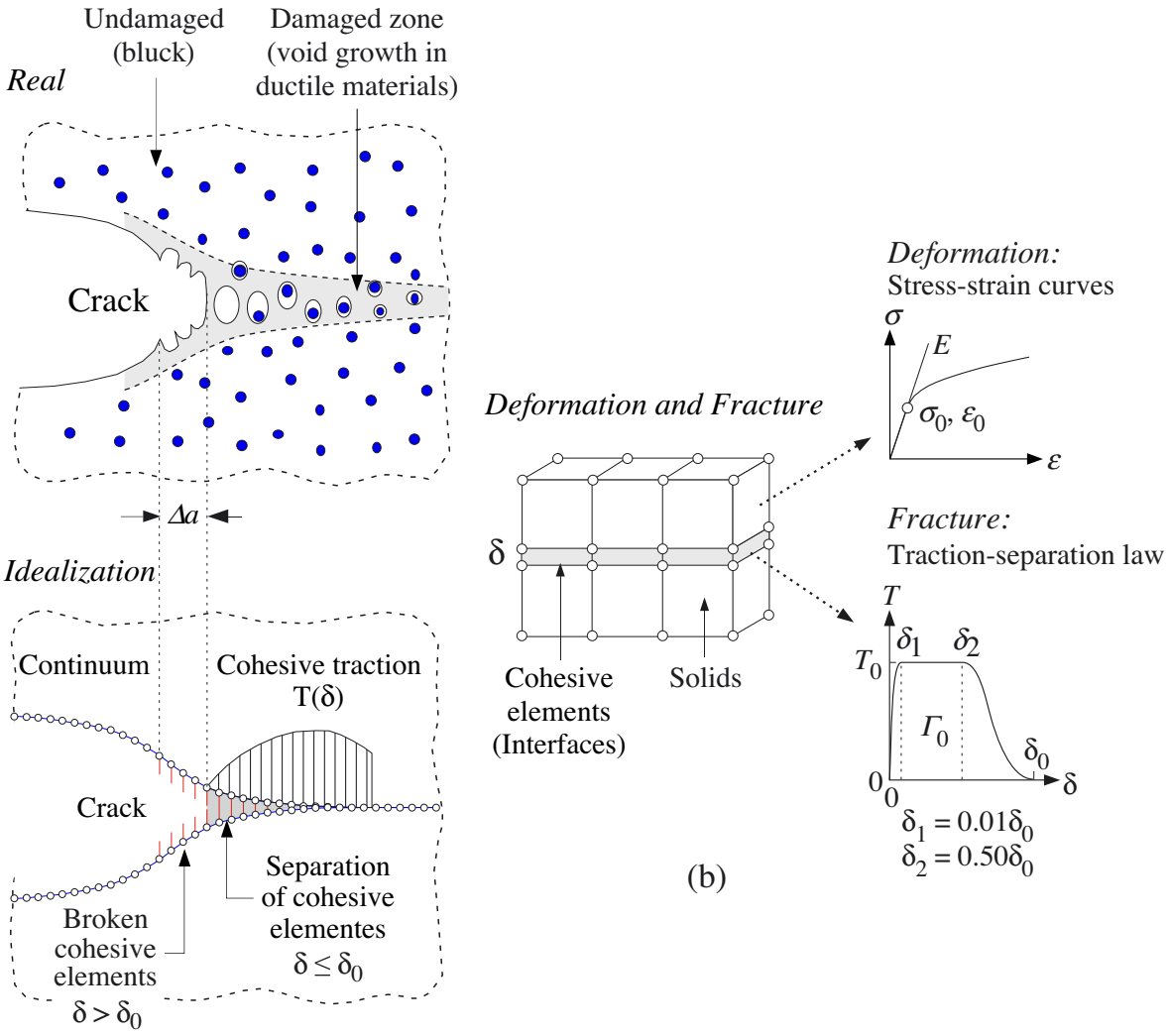
Undamaged
(bluck)
Damaged zone
(void growth in
ductile materials)
Real
Crack
Δa
Idealization
Continuum
Cohesive traction
T(δ)
Crack
Separation
of cohesive
elementes
δ ≤ δ0
Broken
cohesive
elements
δ > δ0
(a)
Deformation and Fracture
δ
Cohesive
elements
(Interfaces)
Solids
Deformation:
Stress-strain curves
σ
E
σ0, ε0
ε
Fracture:
Traction-separation law
T
δ1
δ2
T0
Γ0
δ0
0
0
δ
δ1 = 0.01δ0
δ2 = 0.50δ0
(b)

Fig. 5

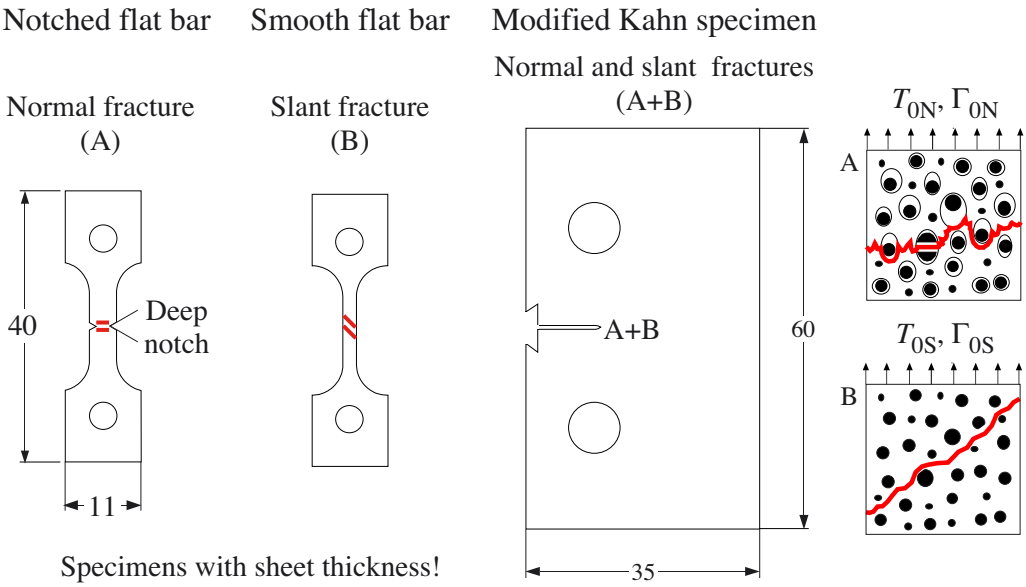
Notched flat bar
Smooth flat bar
Modified Kahn specimen
Normal and slant fractures
(A+B)
Normal fracture
(A)
Slant fracture
(B)
$T_{0N}$, $\Gamma_{0N}$
A
40
Deep
notch
A+B
60
$T_{0S}$, $\Gamma_{0S}$
B
11
35
Specimens with sheet thickness!

Fig. 6

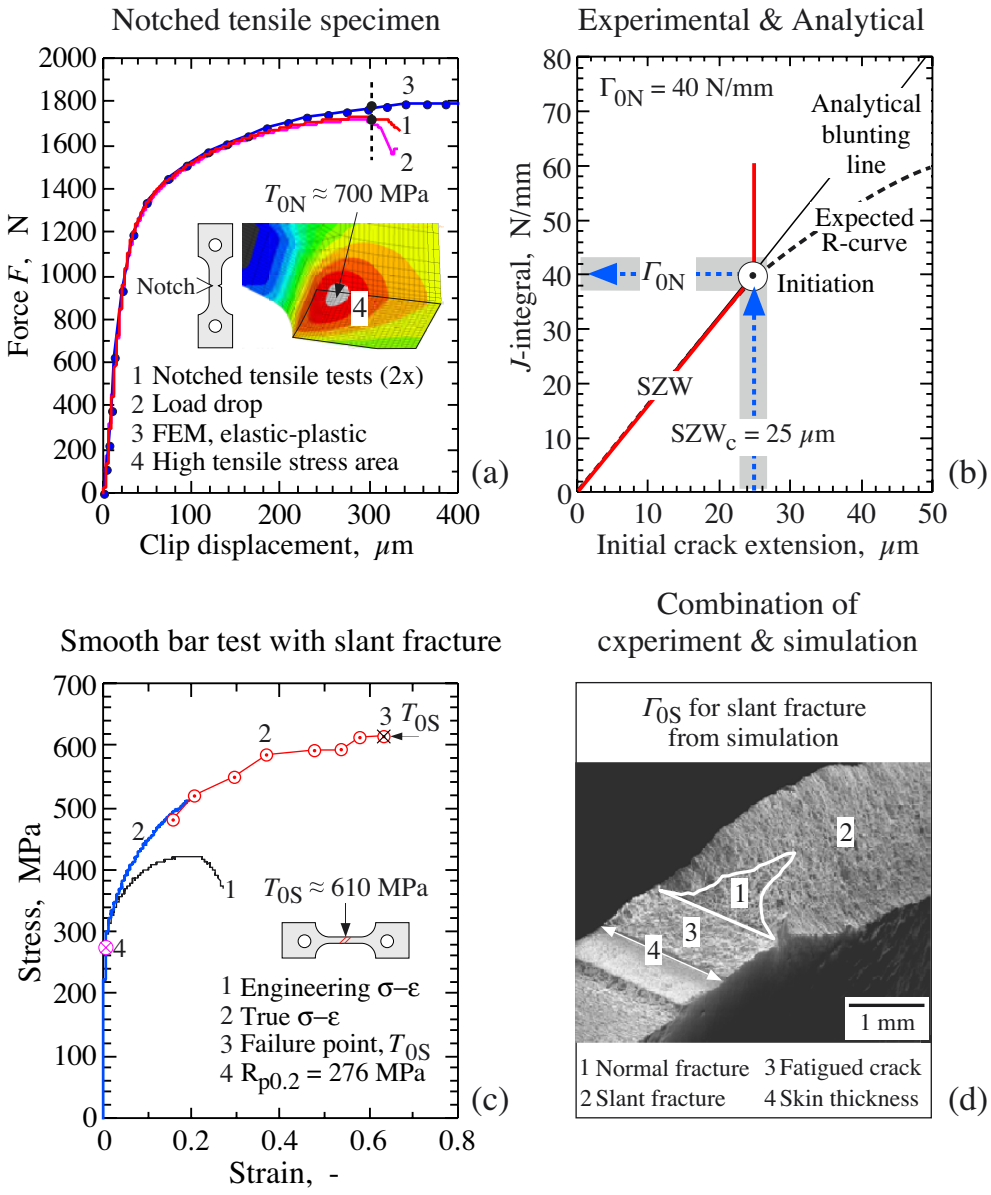
Notched tensile specimen
Force F, N
Clip displacement, μm
T0N ≈ 700 MPa
Notch
1 Notched tensile tests (2x)
2 Load drop
3 FEM, elastic-plastic
4 High tensile stress area
(a)
Experimental & Analytical
J-integral, N/mm
Initial crack extension, μm
Γ0N = 40 N/mm
Analytical blunting line
Expected R-curve
Γ0N
Initiation
SZW
SZWc = 25 μm
(b)
Smooth bar test with slant fracture
Stress, MPa
Strain, -
T0S ≈ 610 MPa
1 Engineering σ–ε
2 True σ–ε
3 Failure point, T0S
4 Rp0.2 = 276 MPa
(c)
Combination of cxperiment & simulation
Γ0S for slant fracture from simulation
1 mm
1 Normal fracture
2 Slant fracture
3 Fatigued crack
4 Skin thickness
(d)

Fig. 7

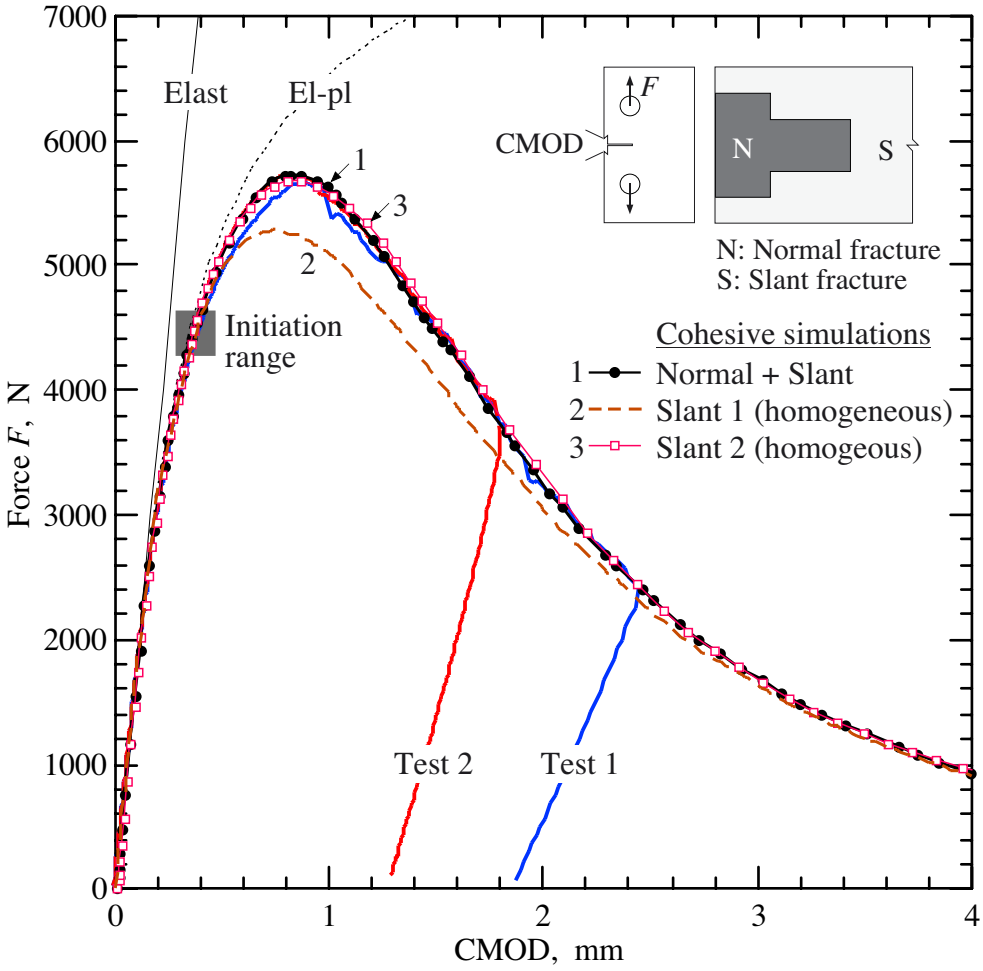
Elast
El-pl
1
2
3
Initiation range
CMOD
F
N
S
N: Normal fracture
S: Slant fracture
Cohesive simulations
1 Normal + Slant
2 Slant 1 (homogeneous)
3 Slant 2 (homogeous)
Test 2
Test 1
Force F, N
CMOD, mm
0
1000
2000
3000
4000
5000
6000
7000
0
1
2
3
4

Fig. 8

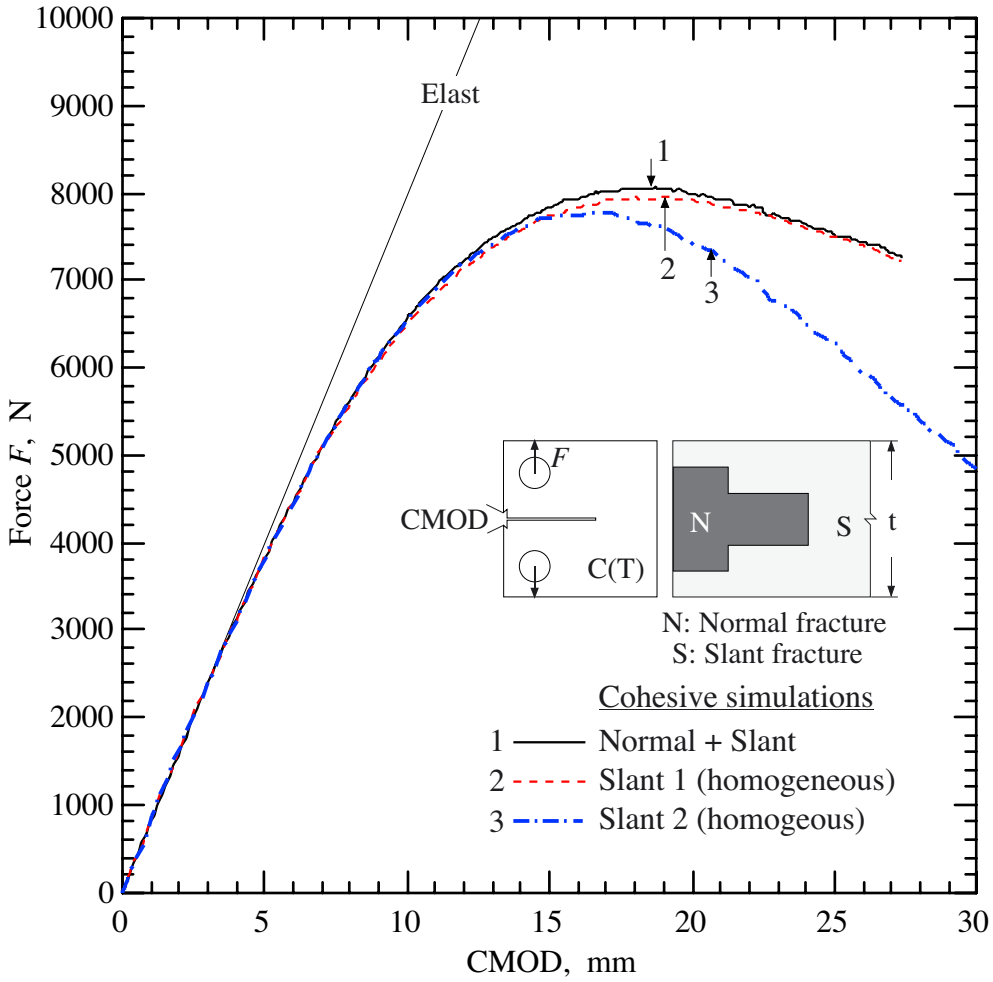
10000
9000
8000
7000
6000
5000
4000
3000
2000
1000
0
Force F, N
0
5
10
15
20
25
30
CMOD, mm
Elast
1
2
3
F
CMOD
C(T)
N
S
t
N: Normal fracture
S: Slant fracture
Cohesive simulations
1 Normal + Slant
2 Slant 1 (homogeneous)
3 Slant 2 (homogeous)

Fig. 9

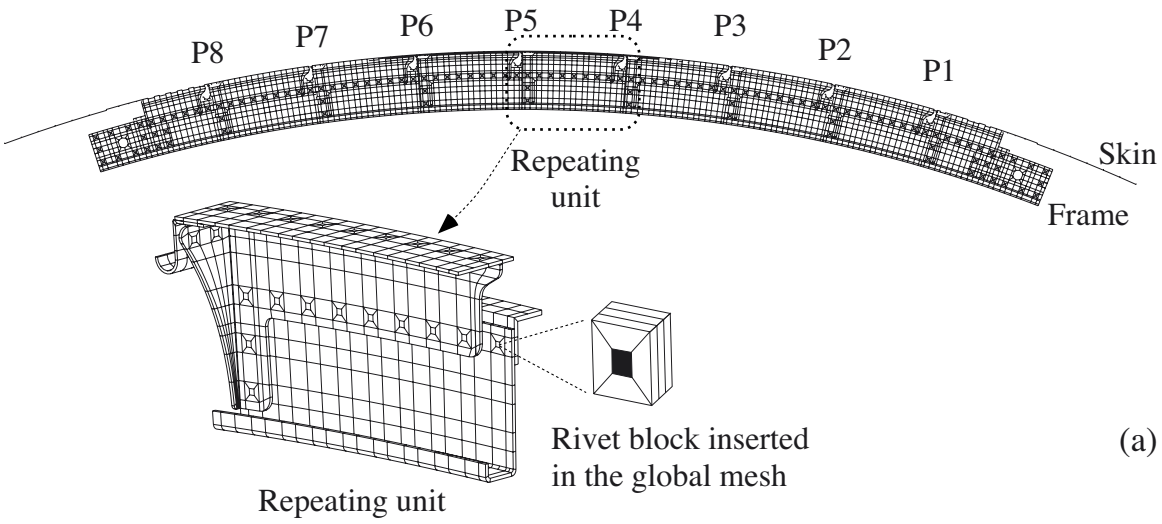
P8
P7
P6
P5
P4
P3
P2
P1
Skin
Frame
Repeating unit
Rivet block inserted in the global mesh
Repeating unit
(a)

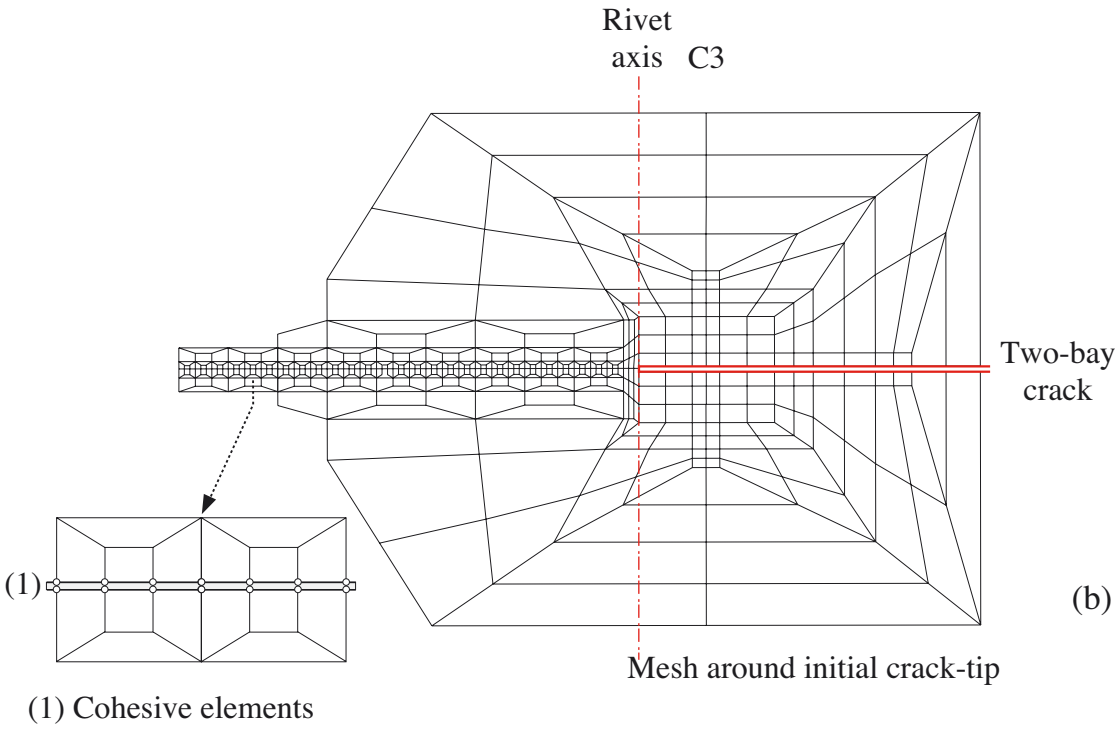
Rivet axis C3
Two-bay crack
(1)
(b)
Mesh around initial crack-tip
(1) Cohesive elements

Fig. 10

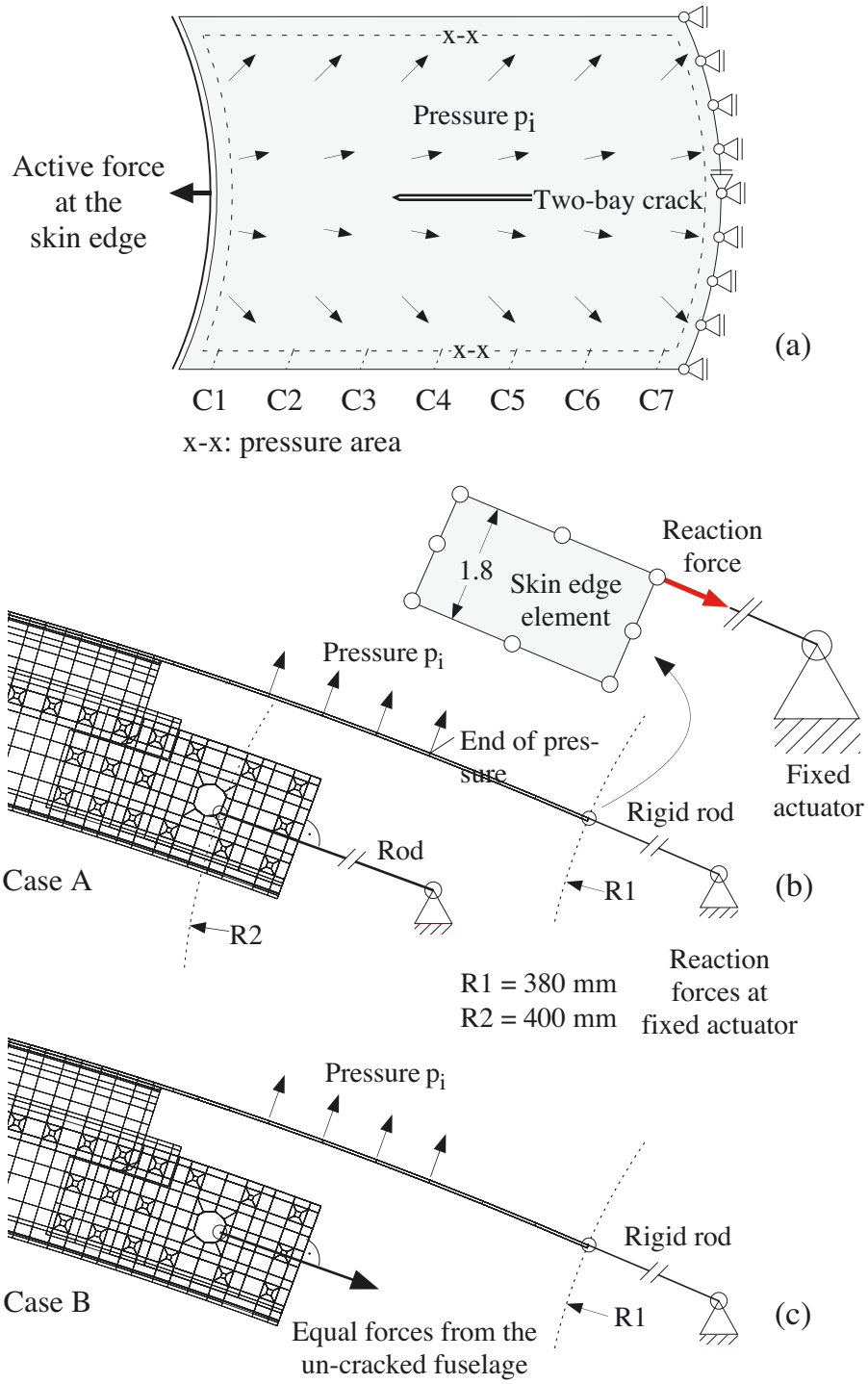
x-x
Pressure $p_i$
Active force
at the
skin edge
Two-bay crack
x-x
(a)
C1 C2 C3 C4 C5 C6 C7
x-x: pressure area
1.8
Skin edge
element
Reaction
force
Pressure $p_i$
End of pres-
sure
Rigid rod
Fixed
actuator
Rod
Case A
R1
(b)
R2
R1 = 380 mm
R2 = 400 mm
Reaction
forces at
fixed actuator
Pressure $p_i$
Rigid rod
Case B
R1
(c)
Equal forces from the
un-cracked fuselage

Fig. 11

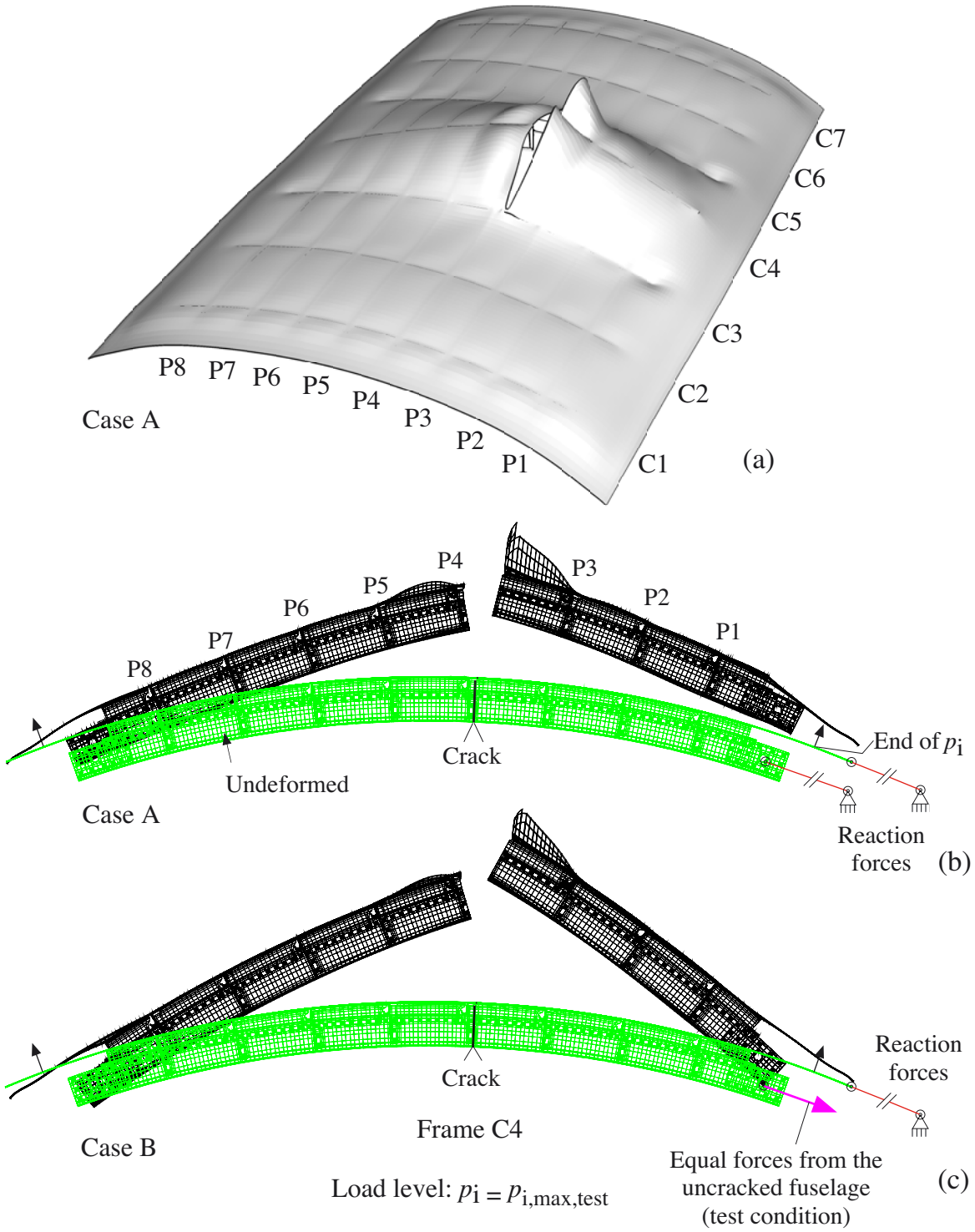
C7
C6
C5
C4
C3
C2
C1
P8
P7
P6
P5
P4
P3
P2
P1
Case A
(a)
P4
P5
P6
P7
P8
P3
P2
P1
End of $p_i$
Undeformed
Crack
Case A
Reaction forces
(b)
Reaction forces
Crack
Frame C4
Case B
Equal forces from the uncracked fuselage (test condition)
Load level: $p_i = p_{i,max,test}$
(c)

Fig. 12

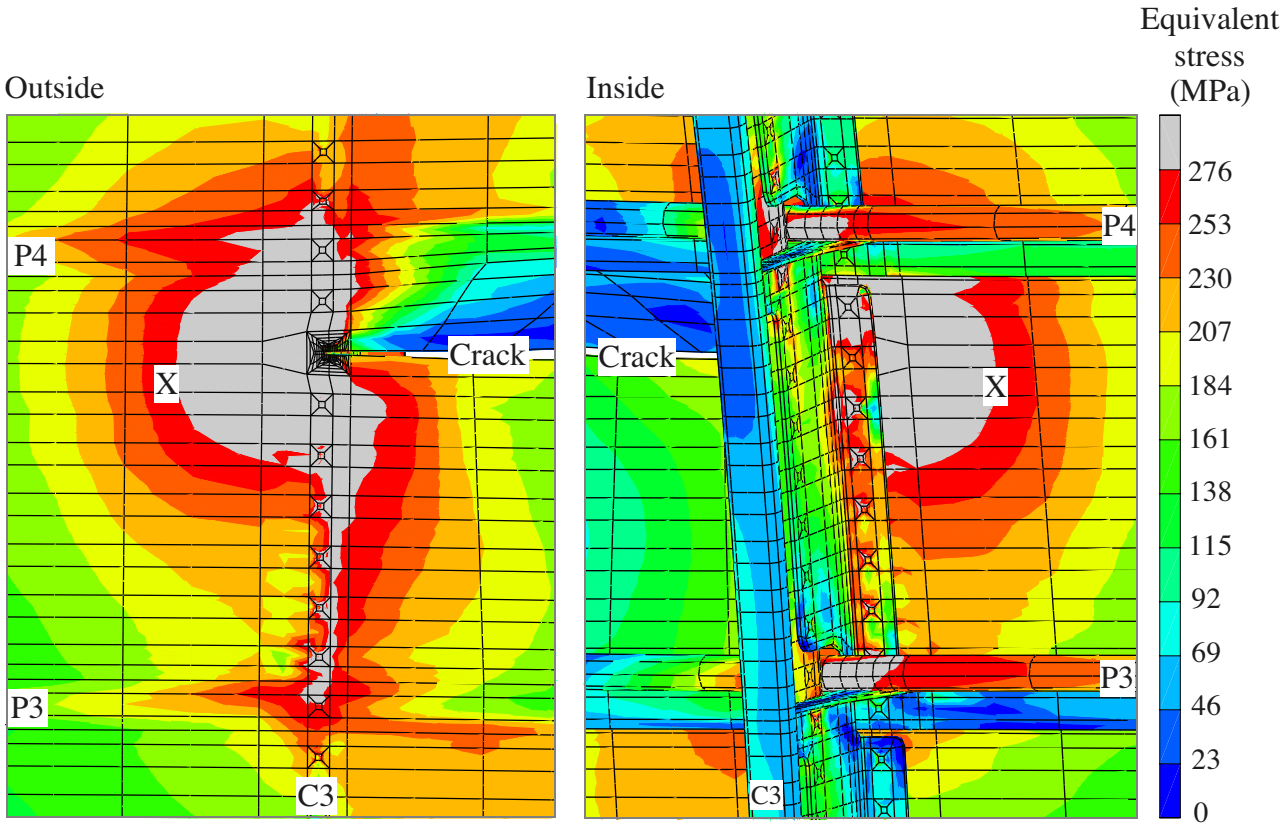


Load level: $p_i = p_{i,max,test}$

(a)

X: Plastic zone border with $R_{p0.2}$ = 276 MPa

(b)

Fig. 13

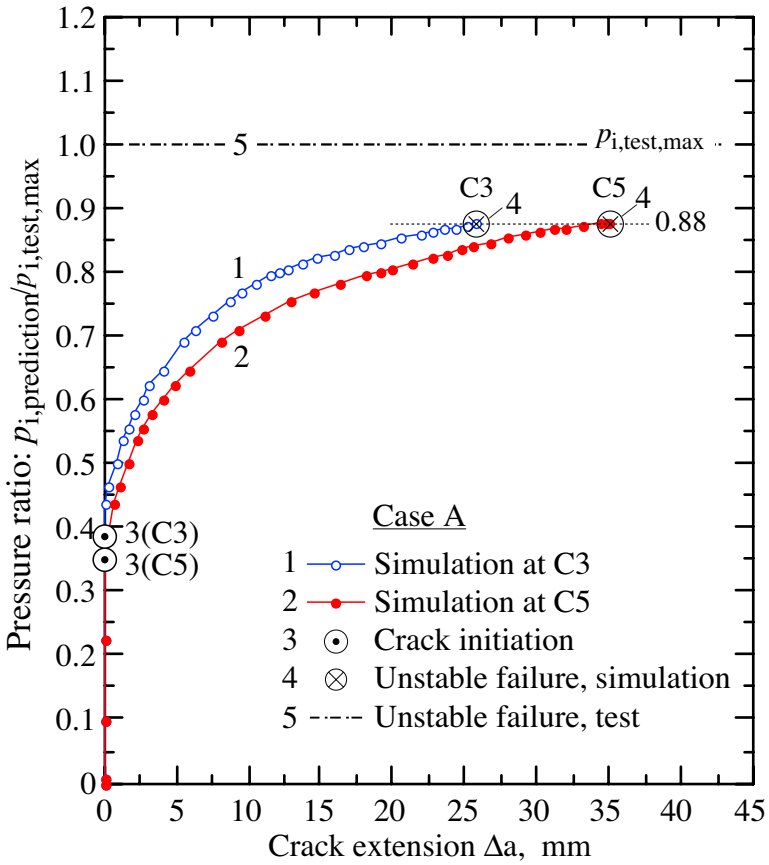
Pressure ratio: $p_{i,prediction}/p_{i,test,max}$
Crack extension Δa, mm
$p_{i,test,max}$
5
C3
C5
4
4
0.88
1
2
3(C3)
3(C5)
Case A
1 Simulation at C3
2 Simulation at C5
3 Crack initiation
4 Unstable failure, simulation
5 Unstable failure, test

Fig. 14

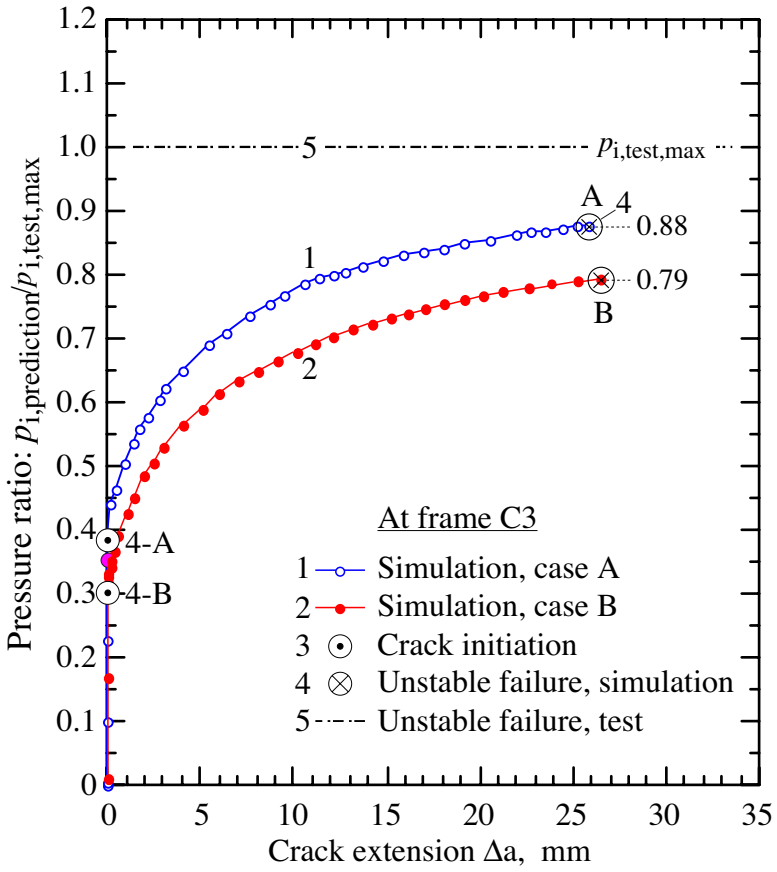
1.2
1.1
1.0
0.9
0.8
0.7
0.6
0.5
0.4
0.3
0.2
0.1
0
0
5
10
15
20
25
30
35
Pressure ratio: $p_{i,prediction}/p_{i,test,max}$
Crack extension Δa, mm
5
$p_{i,test,max}$
A
4
0.88
1
0.79
B
2
4-A
4-B
At frame C3
1 Simulation, case A
2 Simulation, case B
3 Crack initiation
4 Unstable failure, simulation
5 Unstable failure, test

Fig. 15

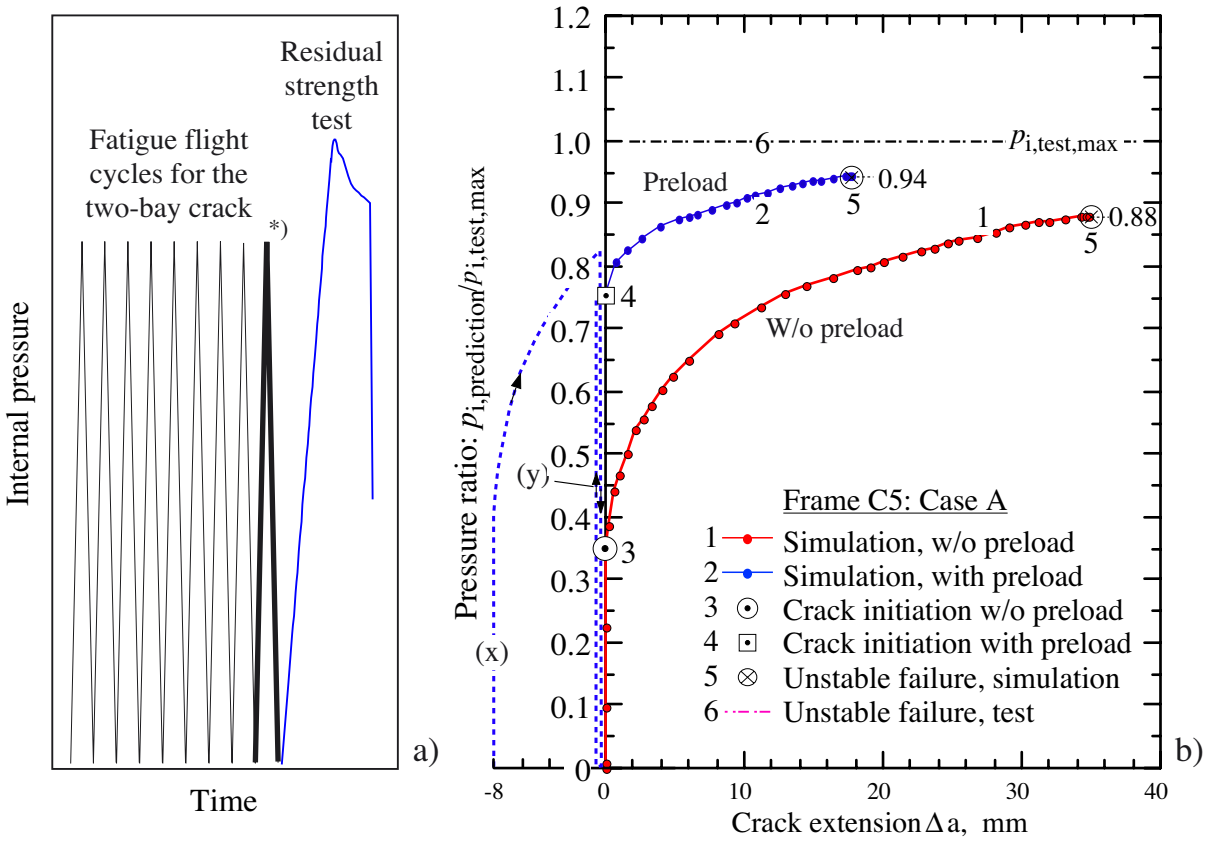


*) Cohesive simulation:
One preloading cycle before static loading; crack-tip starts 8 mm before the frame axes (C3 and C5).

(x) Preloading path until fatigue overload
(y) Unloading and reloading path

Fig. 16